Size Effect on the Tensile Mechanical Behavior of Thin Ti6242S Specimens at 723 K and 823 K

Kevin Cavé, Damien Texier, E. Fessler, D. Monceau, Dominique Poquillon

Size Effect on the Tensile Mechanical Behavior of Thin Ti6242S Specimens at 723 K and 823 K

K. CAVÉ, D. TEXIER, E. FESSLER, D. MONCEAU, and D. POQUILLON

The mechanical behavior of titanium-based alloy Ti6242S was investigated under uniaxial tensile loading at 723 K (450 °C) and 823 K (550 °C) under air and argon environments. Microtensile specimens ranging from 1 mm to 100 μm in thickness were tested to investigate the influence of the decrease in thickness on mechanical properties. Fractographic analyses were carried out using scanning electron microscopy. At 450 °C and 550 °C, a decrease in yield strength, ultimate tensile strength, and strain-to-failure with decreasing thickness was observed. These drops in the macroscopic tensile properties of the thinnest specimens result from a combination of oxidation, which further impairs the specimens with a high surface-to-volume ratio, and the overall lower number of colonies of α lamellae contained in thinner specimens. Ti6242S exhibited dynamic strain aging at 450 °C, especially in specimens with thickness below 500 μm.

I. INTRODUCTION

RECENT developments in digital machining components obtained by topological optimizations and additive manufacturing techniques make it possible to optimize the shape of components with thicknesses down to sub-millimeter dimensions[1] with architectured or thin-walled structures. These new techniques allow reducing mass while keeping good mechanical properties with improved manufacturing costs and decreased raw material consumption. As lightweighting is an efficient way to reduce economic and environmental costs for an industry, the use of size-reduced parts is more and more attractive. However, some applications at high temperature make thin-walled structures particularly sensitive to environmental conditions, such as high temperature oxidation. Size-reduced parts offer a particularly high surface to react with the atmosphere for a reduced volume, thus potentially affecting the mechanical integrity of the structure. Size reduction of components has been intensively studied in the literature.[2–4] For clarity, results from the literature on size reduction effects at room temperature will be first presented to document the effects of free surfaces on the mechanical response of materials with few grains in the thickness. Results of studies on thin films and micropillars will be presented in the second time. Results of studies involving high temperature tests will then be presented underlining the effects of both the free surface and the environment.

At room temperature, size reduction induces a loss of mechanical properties under monotonic tensile stresses for various metals and alloys *i.e.*, pure nickel, copper, aluminum, iron, cobalt, Cu–Al alloy, and nickel-based superalloys.[3–10] While the main tensile macroscopic properties (yield strength, ultimate tensile strength, work-hardening, ductility) remain constant above a given thickness, all these properties decrease when the specimen contains few grains in the thickness. This drop in mechanical properties due to size reduction can be explained by the transition from a polycrystalline behavior to a multicrystalline behavior in the presence of a free surface, as defined by Thompson.[2] These studies considered a difference in mechanical behavior between surface grains and core grains. Hence, the authors generally used the ''thickness/grain diameter'' ratio, t/d, to define their relative contribution in the effective mechanical behavior, which evolves from multicrystalline to polycrystalline when this ratio increases. The polycrystalline to multicrystalline transition can be explained by an increase in the surface-to-volume ratio, with a greater proportion of surface grains as thickness decreases, which gradually impairs the macroscopic mechanical response. Transmission electron microscopy

K. CAVÉ is with the CIRIMAT, Université de Toulouse, CNRS, INP-ENSIACET, 4 Allé de Toulouse, CNRS, INSA, UPS, Mines Albi, ISAE-SUPAERO, Campus Jarlard, 81013, Albi Cedex 09, and also with the SAFRAN Aircraft Engines, Rond-Point René Ravaud, 77550 Moissy-Cramayel, France. Contact e-mail: kevin.cave@ensiacet.fr D. TEXIER is with the Institut Clement Ader (ICA) - UMR CNRS 5312, Université de Toulouse, CNRS, INSA, UPS, Mines Albi, ISAE-SUPAERO. E. FESSLER is with the SAFRAN Aircraft Engines. D. MONCEAU and D. POQUILLON are with the CIRIMAT, Université de Toulouse, CNRS, INP-ENSIACET

(TEM) studies on single crystalline[11,12] and polycrystalline materials[3,5] reported differences between near-surface and core regions as regards mean cell diameter and density of dislocations, due to dislocations escaping through the free surface during loading. This annihilation of dislocations at the free surface results in a softening effect at the macroscopic level. In addition, Miyazaki *et al.*[3] found that specimen geometry can influence the critical thickness at which the polycrystalline to multicrystalline transition occurs. This is due to the difference in surface-grain fraction when comparing flat and cylindrical specimens. Romain *et al.*[10] investigated the impact of environment with tensile tests performed on pre-oxidized specimen. They found a decrease of yield strength, ultimate tensile strength, and ductility due to pre-oxidation treatments linked with oxidation-affected thickness vs specimen thickness ratio. This drop is attributed to the external brittle chromia layer, internal oxidation with alumina spikes, and a ductile γ' precipitates free-layer.

At the sub-micron scale, studies on nickel and gold micropillars reveal an increase of strength (CRSS, yield strength) by diameter decreasing, which is in disagreement with results exposed above.[13–16] Tests performed on thin metal films reveal also higher mechanical properties than polycrystalline metals[17–21] with microbeam deflection techniques, for example. Micro- and sub-micromechanical testing evidence the fact that "smaller is stronger" due to dislocations starvation and to the difficulty to generate new dislocations in such small volumes. This mechanism highlights the competition between dislocations multiplication before annihilation at free-surface level. In case of non-multiplication of dislocations, a greater stress level is necessary to activate dislocation sources and accommodate straining. Benzarga and Shaver[22] has proposed a model with constitutive equations with a physical representation of dislocations sources to represent this size effect. In the case of thin films, this strengthening can be explained by constraints on dislocation motion such as grain boundaries in Venkatraman and Bravman work[23] and substrate used in Nix work.[17] Passivation, *i.e.*, the presence of a thin oxide film, seems to strengthen the mechanical behavior of thin Cu films at 600 °C, as showed by Keller *et al.*[18]

For high temperature micromechanical testing, exposure of specimen to air may cause surface properties to change due to oxidation. Studies on the creep of single-crystal nickel-based superalloys at high temperature in air or vacuum reveal a decrease in creep strength with decreasing thickness, associated with phase transformation under the external oxide layer.[24–26] To explain this thickness debit, Cassenti *et al.*[26] defined a peripheral damaged layer induced by extrusion–intrusion mechanisms (at microscopic scale) at the surface of the nickel-based single-crystal superalloy due to the ratio between dislocation loop diameter and specimen thickness. These authors demonstrated their experimental findings through numerical calculations. They showed that microscopic surface mechanisms, including oxidation, might have a significant effect on the macroscopic response of thin-walled single-crystal specimens under creep due to a greater surface-to-volume ratio. In addition, oxidation can lead to modifications in the bulk of the material. Indeed, Brunner *et al.*[25] evidenced the formation of γ'-free zones prone to void nucleation[24] and a modification in the matrix microstructure with a reduction in the γ' volume fraction. For thinner specimens, oxidation can affect the whole section of the specimen. Observations of fracture surfaces reveal a mixed mode of cleavage-like facets and dimples with an increase in cleavage area proportion due to thickness reduction.[24] Moreover, in the case of titanium and titanium-based alloys, oxidation leads to the formation of an oxide layer plus an oxygen-enriched layer beneath the external oxide scale due to high oxygen solubility in titanium. This dissolution of oxygen increases mechanical properties such as hardness,[27,28] yield strength,[27,29–31] ultimate tensile strength,[27,30,32] and the magnitude of the critical resolved shear stress value for the different slip systems.[33] Chong *et al.*[34] show that a low amount of oxygen ($\leq$ 0.3 wt pct) is sufficient to induce an increase of ultimate tensile strength, yield strength, and a ductility decrease with oxygen content. This could affect dislocation motion and modify the surface of titanium alloys during high temperature tensile tests even under non-oxidizing atmospheres. Oxidation also decreases alloy ductility.[27] Avoiding the oxidation of Ti-based alloys exposed to high temperatures is rather difficult as it requires a very low oxygen partial pressure according to the Ellingham diagram.[35] It is therefore very challenging to study thickness effects of Ti-based alloys at high temperature without environmental/oxidation contribution. To the authors' knowledge, size effects at high temperature have not been studied in Ti-based alloys regardless of the environmental conditions. Microsample tensile testing was yet performed on single crystals of γ-Ti–Al alloys in works by Zupan *et al.*[36,37] Environmental conditions, especially temperature, constitute limiting conditions for the use of Ti-based alloys. Indeed, at temperatures above 540 °C, Ni-based alloys are used[38] due to oxygen embrittlement of Ti-based alloys under fatigue and creep conditions. Currently, Ti–6Al–4V is the most widely used titanium alloy to manufacture aeroengine components exposed to temperatures below 315 °C.[38] Ti6242S alloy is used at higher temperatures as it presents higher mechanical performances.[39] The present study focuses on the behavior of thin specimens of alloy Ti6242S during tensile tests at 450 °C and 550 °C. Indeed, these temperatures are of interest for aeroengine applications. Specimens with different thicknesses ranging from 100 μm to 1 mm were tested under air conditions and high-purity argon to study the consequences of thickness decrease and surface modification on the mechanical response due to slight oxidation.

II. MATERIAL AND METHODS

The as-received Ti6242S alloy was provided in the form of a forged disk and exhibited a Widmanstätten microstructure with α lamellae (width of 2–3 μm), as presented in Figure 1. Morphological parameters of α colonies were measured using electron backscattered diffraction (EBSD). α colonies displayed an average

width of 30 μm. In addition, EBSD analyses using variants analyses aimed to evaluate parent β-grain size of 500 μm width and several millimeters in length. Table I describes the chemical composition of the Ti6242S alloy obtained using Inductively Coupled Plasma Optical Emission Spectroscopy (ICP-OES) for major metallic elements, Glow Discharge Mass Spectrometry (GDMS) for metallic impurities, and Instrumental Gas Analysis (IGA) for gaseous species by EAG Laboratories (France). Microtensile specimens were extracted from the disk using electrodischarge machining. The longitudinal direction of the microtensile specimens is aligned with the circumferential direction of the disk. The gage area of these specimens is 5 mm long and 2.5 mm wide. Specimens were prepared by mechanical polishing using a precision jig following the method described in Reference 40. Microtensile specimens were ground and polished with SiC paper down to P2400 grade. This gentle mechanical technique aimed at minimizing the residual stresses inherent to the preparation. Four thicknesses were investigated in the present study *i.e.*, 1 mm, 500 μm, 250 μm, and 100 μm, in order to characterize size effect on the mechanical response. The equivalent grain diameter, d, was here considered as the colony average width of 30 μm, due to change in orientation from colony to colony and potentially slip activity as highlighted in Reference 41 for a Ti–6Al–4V-alloy with a bimodal microstructure. In this work on bimodal microstructure, Lunt *et al.*[41] highlighted that strain partitioning occurs between α nodules and grains with Widmanstätten microstructure. They evidenced using high-resolution-digital image correlation (HR-DIC) that the length of strain localization features is in the order of the colony diameter and lath length. They observed slip localization confined within individual colonies with plastic events occurring either in a trans-lamellae manner or parallel to interfaces. This result supports the hypothesis that the colony size is the relevant length regarding slip activity in the Widmanstätten microstructure. The t/d ratio varies from 33 for 1-mm thick specimens to 3 for 100-μm thick specimens considering α colonies as strengthening barrier (d = 30 μm). Specimen thickness was measured at 5 positions along the specimen length using a micrometer with a precision of 1 μm. With this polishing technique, a variation of less than 2 μm was measured over the whole gage length. For the thinnest specimens, this corresponds to a section variation of less than 2 pct.

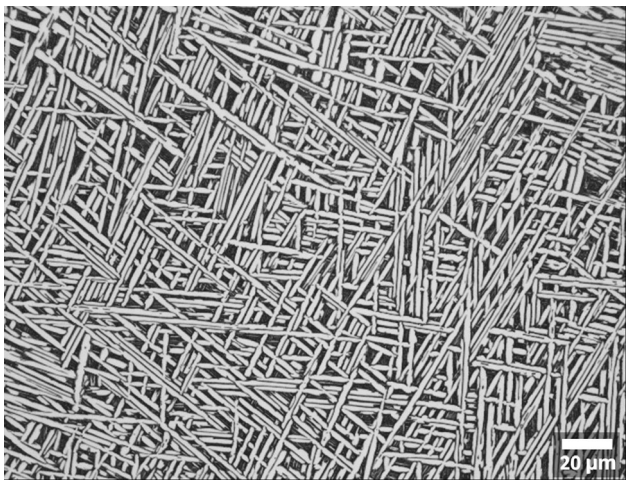

Fig. 1—Ti6242S alloy microstructure observed using optical microscopy after Kroll etching.

Tensile tests were conducted using an electromechanical MTS tensile machine equipped with a 5 kN load cell. Two tests per condition were performed to ensure reproducibility, except for 500 μm specimens in argon. For tests carried out in air, one test was interrupted at the beginning of specimen necking *i.e.*, at the ultimate tensile strength. As UTS depends on specimen thickness, the tests were stopped at different deformation levels. A constant crosshead displacement rate was maintained during tests at 5.10^{-5} mm s^{-1}, corresponding to a strain rate of 10^{-5} s^{-1}.

Tensile tests were paired with the digital image correlation (DIC) technique using full-field measurement to assess kinematics field at the mesoscopic level in the gage area. DIC was used as an optical extensometer to address macroscopic behavior. The pixel-to-millimeter ratio is equal to 256 pixels/mm. Prior to tensile tests, a white speckle (alumina powder) was sprayed on the microtensile specimens forming a speckle pattern with sparsely distributed particles. Displacement and strain in the loading direction (ε_{yy}) were computed using the VIC software algorithm from Correlated Solutions.[42] The average value of ε_{yy} was determined for every image sequence and used to plot the stress–strain evolution during tensile loading after synchronization of the load/picture data. Particular care was taken in the gripping of specimens; the technique is presented in Reference 32. In addition, the displacement between the two grips was measured using a KEYENCE LS7030M optical micrometer. Special attention was paid to the alignment of each microtensile specimen before tests. Tensile tests were conducted at 450 °C and 550 °C. The temperature was controlled and verified using 3 type-K thermocouples welded on a sacrificial specimen (i) to ensure a gradient lower than 2 °C on the whole gage length and (ii) to avoid damaging the microtensile specimen. The heating device is a three-zone halogen lamp furnace

Table I. Chemical Composition of Alloy Ti6242S (Weight Percent). Ti, Al, Zr, Mo, and Sn Elements Were Quantified Using ICPOES, IGA for O, N, and C and GDMS for Fe and Si

Elements	Ti	Al	Sn	Zr	Mo	Si	Fe	O	N	C
Weight Percent	bal	5.8	2.0	4.3	1.9	0.1	0.02	0.12	0.002	0.006

controlled by three PIDs. A thermal calibration was performed before the tensile test campaign to validate this method. A constant load lower than 150 MPa, *i.e.*, below 15 pct of YS, was applied during the heating procedure and temperature dwell so that the specimen remains in tension. This low load level has been chosen in order to get a negligible viscoplastic strain during heating according to creep data available in the literature for Ti6242S. A dwell time of 1 hours prior to tensile testing was applied to ensure thermal stability. A "load-unload-load" sequence was performed during the tensile tests in order to measure the Young modulus during the unloading step. Tensile experiments were performed at 450 °C and 550 °C under both air and high-purity argon atmosphere to investigate the effect of oxidation during tensile experiments. Tests with the longest duration at 550 °C exposed alloy Ti6242S to oxidation for 2 hours. This induced the formation of a 19-nm-thick oxide scale and an oxygen-enriched layer of 0.7 μm according to the model put forward by Vaché *et al.*[43]

The impacts of thickness decreasing and environment on yield strength (YS), (resp. UTS) are investigated through normalization with a stress value strength corresponding to the maximum YS, denoted S_p, for thicker specimens (resp. UTS, S_m) tested under air environment. YS corresponds to the 0.2 pct offset yield.

XRD characterization was conducted at room temperature with a Bruker D8 GIXRD at low incidence angle (1° and 5°) and with a Bragg's angle in the 2θ range from 20° to 80° using a step size of 0.02° and a scan step time of 2 seconds. This analysis confirmed that the oxide scale was made of anatase. In the case of the thinnest specimens (100 μm), the enriched area corresponding to the oxygen-enriched alloy represents less than 1 pct of the initial section using diffusion model in Reference 43. Even though this represents a small proportion of the total area, this oxidation might affect surface mechanisms, especially damage initiation. In order to investigate the impact of this oxidation on the mechanical behavior, some tensile tests were also conducted under static slightly overpressured high-purity argon (99,999 pct) with less than 2 ppm of O_2, 5 ppm of N_2, and 3 ppm of H_2O. A secondary vacuum was first performed in the furnace. Then the furnace was filled with argon. This vacuum/Ar filling sequence was repeated two additional times at 150 °C in order to decrease the level of residual oxygen (adsorbed H_2O and O_2). The furnace was then filled with high-purity argon. A check valve was installed to maintain a 500 mbar overpressure throughout the tests.

Fractographic analyses were performed using a ThermoFisher Scientific Quanta 450 scanning electron microscope (SEM) at 10 kV. The dimpled area and the size of the dimples were measured using the ImageJ software.[44] For each fractured specimen, its width variation was measured using a Keyence CV-H500C camera focused on the whole gage length at various distances from the fracture surface. Strain-to-failure (STF) was calculated measuring the minimum section at necking and applying the assumption of volume conservation during plastic deformation with $= ln(\frac{S_0}{S_{broken}})$.

III. RESULTS

A. *Influence of Specimen Thickness at 450 °C*

True tensile stress–strain curves obtained for different specimen thicknesses under air and under argon environments are presented in Figures 2(a) and (b), respectively. First, a similar elastic behavior is observed for all thicknesses under both environments. The values of Young modulus for each thickness are summarized in Table II. The yield strength depends on specimen thickness and decreases with decreasing specimen thickness. For a 100-μm-thick specimen, the yield strength is slightly lower for tensile experiments performed under air environment *i.e.*, at approximately $0.77 \times S_p$ under air and $0.87 \times S_p$ under argon. For a 250-μm-thick specimen, normalized YS is greater in air than in argon environment. For thicker specimens, the yield strength (resp. UTS) is greater (resp. lower) under air than under argon environment, as depicted in Figure 3(a). The variation of normalized ultimate tensile strength with thickness is presented in Figure 3(b). Under air, variations of YS and UTS are evidenced for 1 mm to 500-μm-thick specimens but a significant decrease of both YS and UTS was found for thinner specimens. As specimen thickness decreases from 1 mm to 100 μm, YS (resp. UTS) drops by 22 pct (resp. 21 pct). YS (resp. UTS) drops by 15 pct (resp. 5 pct) when thickness decreases from 250 μm to 100 μm. In comparison, under argon environment, results show a decrease in macroscopic mechanical properties: as thickness decreases from 500 to 250 μm, yield strength drops by 5 pct and ultimate tensile strength by 10 pct. The tendency observed under air is confirmed under argon between 250 and 100 μm but the drop is lower: a 1 pct drop in yield strength and 4 pct drop in ultimate tensile strength. This drop in YS and UTS with thickness decreasing is larger when tests are performed under air compared to those carried out under argon environment.

By comparing the results obtained for each environment, it can be noted that, for the thinnest specimens (250 μm and 100 μm), normalized UTS and YS values increase when switching from air to argon. Thicker specimens are not impacted by this atmosphere switch. The plastic domain exhibits serrations due to dynamic strain aging (DSA) for 500, 250, and 100-μm-thick specimens tested under argon. These serration amplitudes were found 25 to 5 times greater than the load cell noise for 500-μm to 100-μm-thick specimens. For 1 mm and 500-μm-thick specimens, no serrations were evidenced under air environment, as shown in Figure 2. The serrations are characterized by the magnitude of the load drop in comparison to the previous level. The strain at the onset of serrations, ε_c, the mean amplitude value, and frequency are also analyzed with the peak findings function of the SciPy Python package. The determined parameters are summarized in Table III for each tested thickness. Under argon, as thickness increases, the average value of ε_c increases from 1.4 ± 0.2 pct for 100 μm to 1.5 ± 0.1 pct for 250 μm and to 2.4 pct for 500 μm. Under air environment, this value increases from 1.7 ± 0.5 pct for 100 μm to

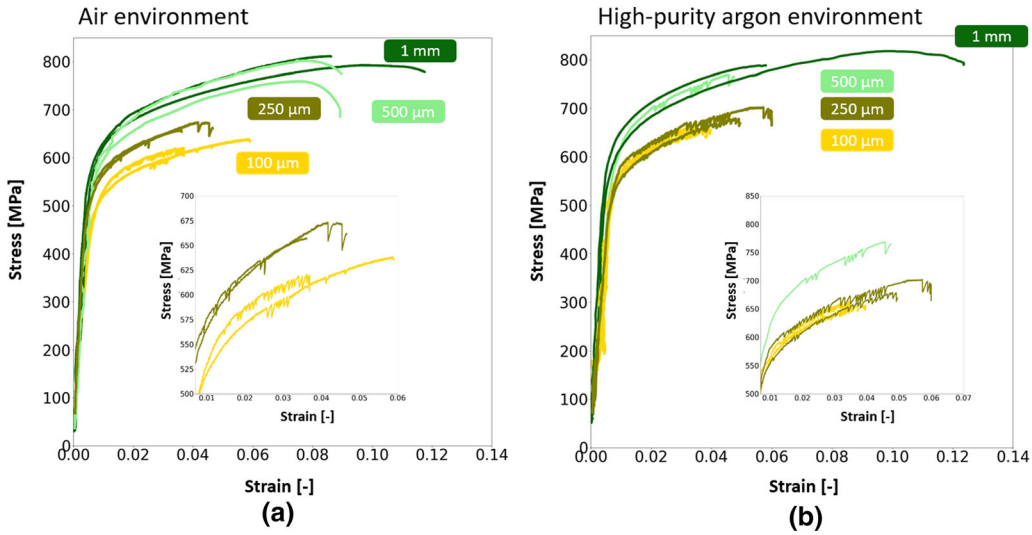

Fig. 2—True stress–strain curves at 450 °C under air (*a*), under high-purity argon (*b*) and serrated behavior for different specimen thicknesses.

Table II. Young Modulus Values (in GPa) Determined at 450 °C for Each Thickness as a Function of Environment During Unloading

	1 mm	500 µm	250 µm	100 µm
Air	102	103	100	102
Argon	98	104	102	103

Young modulus determination technique induces error that can reach 4 GPa.

figure clearly shows a significant drop in ductility with decreasing specimen thickness, about 15 pct comparing 1 mm and 100 µm specimens. Given these results and from Figure 4(b), it seems that strain-to-failure is similar whichever the environment for all tested thicknesses.

Kinematics fields from DIC measurement were also used to study the local scale impact of decreasing thickness. At $\varepsilon = 0.4$ pct, strain distribution is found homogeneous for all specimens tested regardless of thickness. Strain distribution along the gage area was

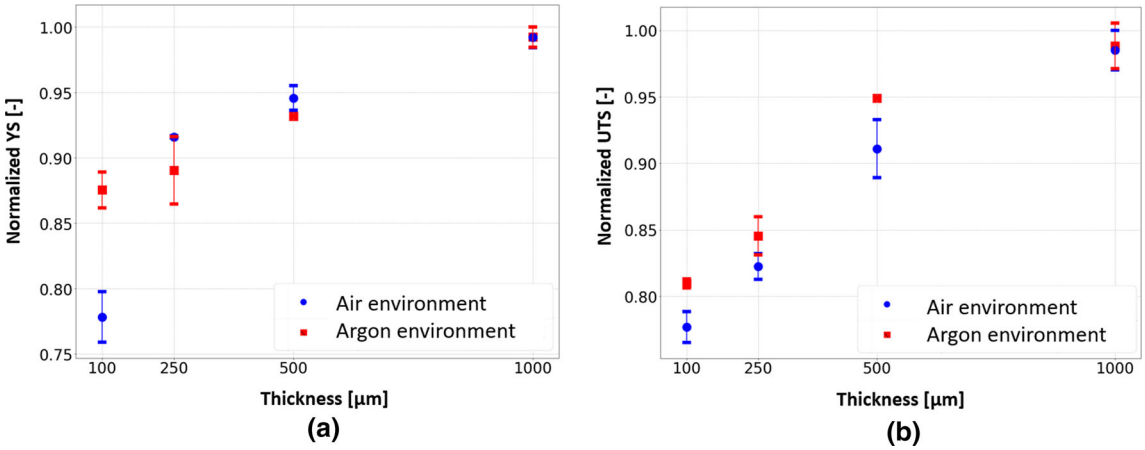

Fig. 3—Evolution of normalized Yield Strength (YS) (*a*) and Ultimate Tensile Strength (UTS) (*b*) at 450 °C as a function of specimen thickness under air and under high-purity argon. The error bars correspond to the experimental dispersion of YS and UTS.

2.3 ± 1.6 pct for 250 µm. The mean value of stress drop increases from 9 MPa for 100 µm to 12 MPa for 500 µm under argon. The frequency of serrations also increases with decreasing thickness and by changing atmosphere from air to argon environment.

The impact on ductility is evaluated through the variation of width (related to section variation) over the whole gage length. Widths are measured on the failed specimens and results are presented in Figure 4. This investigated for all the specimens but a particular focus on two thicknesses was done for comparison: 250-µm- and 1-mm-thick specimens. While strain distribution remained homogeneous for the 1-mm-thick specimen before necking, an inclined band exhibiting higher strain values developed across the gage width above yielding for the 250-µm-thick specimen. This localization band oriented at approximately 60 deg to the loading axis appears for strain level lower than the critical strain for

serration onset for one 250-μm-thick specimen tested in air. In the other conditions in both atmospheres, localization bands appear for strain level close to the one for serration onset. For thinnest specimens, failure is observed in the vicinity of this early localization band.

B. *Influence of Specimen Thickness at 550 °C*

True tensile stress–strain curves obtained at 550 °C are presented in Figure 5. Under both environments, the elastic behavior is not influenced by a decrease in thickness. The values of Young modulus for each thickness are summarized in Table IV. For a 100-μm-thick specimen, the yield strength is slightly lower for tensile experiments performed under air environment, *i.e.*, at approximately $0.71 \times S_p$ under air and $0.78 \times S_p$ under argon. For 1-mm-thick samples, the yield strength is greater in air than in argon (+ 6 pct). The opposite trend is found for the UTS. The study of normalized YS and UTS reveals a drop of 25 pct in normalized yield strength and 32 pct in normalized ultimate tensile strength when specimen thickness decreases from 1 mm to 100 μm, as displayed in Figures 6(a) and (b). When specimen thickness decreases from 500 to 250 μm, a decrease of 5 pct in yield strength and 4 pct in ultimate tensile strength under argon environment is highlighted, as displayed in Figure 6. From 250 to 100 μm, the drop in yield strength and ultimate tensile strength is about 5 and 4 pct, respectively. When comparing the results obtained under both atmospheres, the drop in mechanical properties (yield strength and ultimate tensile strength) is greater under air than under argon as thickness decreases. Plastic behavior before necking is comparable under both environments for all thicknesses tested. Under both atmospheres, no serrated behavior was observed.

At 550 °C, strain-to-failure decreases with decreasing thickness. An increase in strain-to-failure with specimen thickness can be observed as temperature increases, which is in good agreement with the increase in tensile ductility with temperature observed in titanium alloys.[45,46] The drop in strain-to-failure increases with temperature under both atmospheres. In Figure 4(c), no difference can be noticed between strain-to-failure obtained under argon and air.

At the local scale, strain distribution is homogeneous for all specimens tested below 0.8 pct total strain. For 250-μm-thick specimens, strain distribution stays homogeneous between 0.8 and 1.5 pct as for 1-mm-thick specimens. Strain localization begins to appear for strain levels above 1.5 pct and becomes more and more intense with loading. Interestingly, both thin and thick specimens were less sensitive to localization bands at 550 °C compared to 450 °C, and no serrations were observed in the plastic domain.

C. *Fractographic Analyses*

Figures 7 and 8 show the fractographies of specimens tested at 450 and 550 °C. At both temperatures, the aspect of the fractographies does not change whichever the specimen thickness. All fracture surfaces exhibit dimples, interlamellar fracture features, and area reduction due to necking. The areas dominated by dimples and fractures were measured and compared. Dimples were localized in the core of the samples. The fraction of the area dominated by dimples slightly decreases from 66 pct for 500-μm-thick specimens to 60 pct for 100-μm-thick specimens.

Gage sections were measured for each thickness and compared to the initial section, prior to tensile testing. The comparison between 500-μm-thick specimens tested at 450 °C and 550 °C revealed a decrease in the ratio between the failed and the initial gage section (FIGS ratio) of 58 and 53 pct, respectively. As expected, the ductility of the alloy is higher at 550 °C than at 450 °C.

For a given temperature, this analysis reveals that the FIGS ratio increases as thickness decreases, varying from about 58 pct (500 μm) to 74 pct (100 μm) at 450 °C and from about 53 pct (500 μm) to 62 pct (100 μm) at 550 °C. Thinner specimens are locally less strained than thicker ones. Dimple size was measured using the intercept method used for grain size measurements. The mean size of the dimples decreases with specimen thickness: at 450 °C, their size reaches 2.76 ± 0.33 μm for 500-μm and 1.86 ± 0.25 μm for 100-μm specimen.

SEM observations of specimens tested under argon environment reveal features similar to those observed on specimens tested under air environment. In both cases, SEM observations of the surface of the specimens were also performed. They revealed the presence of cracks not only near the fracture surface but also a few millimeters away from it. The cracks are often perpendicular to the loading direction. Therefore, their orientation does not depend on the microstructure of the material and especially not on the morphological orientation of its lamellae. Shear lips can be seen on Figure 8(b) and (e).

The surface of specimens was also observed using optical microscopy, which evidenced a change of color due to specimen oxidation. For the thinnest samples (250 and 100 μm), these observations revealed a metallic aspect for specimens tested under argon, whereas those tested under air had a homogeneous blue color.

IV. DISCUSSION

Investigation of mechanical behavior performed at both temperatures and atmospheres demonstrated a decrease in mechanical strength as specimen thickness decreased. This drop in mechanical strength for thinner specimens increases with temperature and decreases with Ar atmosphere as compared to air. Two phenomena can explain these results:

- A decrease in the number of colonies of α lamellae through the thickness of Ti6242S specimens, as in polycrystalline structures, and an increase in the surface-to-volume ratio as specimen thickness decreases;
- A slight oxidation of the specimen during tensile tests under both atmospheres leading to an

Table III. Summary of Determined DSA Parameters as a Function of the Specimen Thickness and Environment at 450 °C

Thickness [μm]	Environment	ε_c	Mean Amplitude [MPa]	Frequency [Hz]
100	air	1.7 ± 0.5 pct	8 ± 4	0.10
250	air	2.4 ± 1 pct	14 ± 5	0.03
100	argon	1.4 ± 0.2 pct	9 ± 3	0.11
250	argon	1.5 ± 0.1 pct	10.3 ± 7	0.05
500	argon	2.4 pct	12 ± 4	0.03

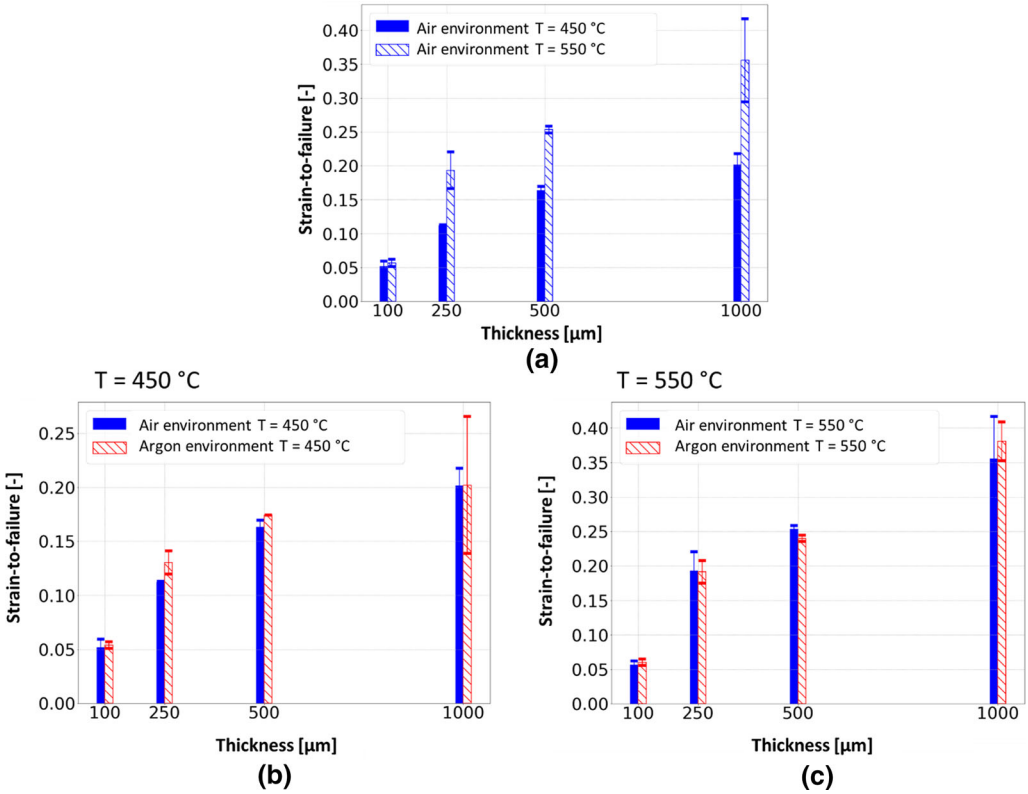

Fig. 4—Variation of Strain-to-Failure (STF) with thickness at 450 and 550 °C (*a*), Variation of STF with specimen thickness under air and argon environment at 450 °C (*b*) and 550 °C (*c*). The error bars correspond to the experimental dispersion of STF.

embrittlement of the material. The oxygen partial pressure in the high-purity Ar atmosphere was not low enough to fully prevent alloy Ti6242S from oxidation. The equilibrium oxygen partial pressure for TiO_2 formation is 10^{-13} at 550 °C according to the Ellingham diagram.[35]

These two points will be discussed in the two subsequent sections. The occurrence of dynamic strain aging (DSA) will be discussed in a third section.

A. *Influence of the Size of α Lamellae Colonies Compared to Specimen Thickness*

A key factor strongly influencing the thickness at which the polycrystalline to multicrystalline transition occurs is the grain size in single-phase materials or small-size precipitation hardened materials.[4,6,47,48] In the present work, the microstructure of alloy Ti6242S is complex and composed of α lamellae with a width of 2–3 μm in the form of a Widmanstätten microstructure (see Figure 1). α colonies were found to have an average width of 30 μm. α colonies size is considered here as the key microstructural characteristic for plastic behavior since strain localization is confined into colonies either trans-lamellae or along α lamellae. This strain localization depends on the crystallographic orientation of the colony regarding the loading direction. Lunt *et al.* have investigated this point on Ti–6Al–4V with bimodal microstructure.[41] Considering the average size of α colonies, the ratio t/d (thickness to grain diameter) described in Reference 5 varies from 3 for 100 μm to 33 for 1 mm specimens. The analysis of mechanical properties variation highlights a size effect at both temperatures with a transition between 500 μm and 1 mm. A decrease in sample thickness increases the ratio of surface colonies to core colonies, thereby increasing the

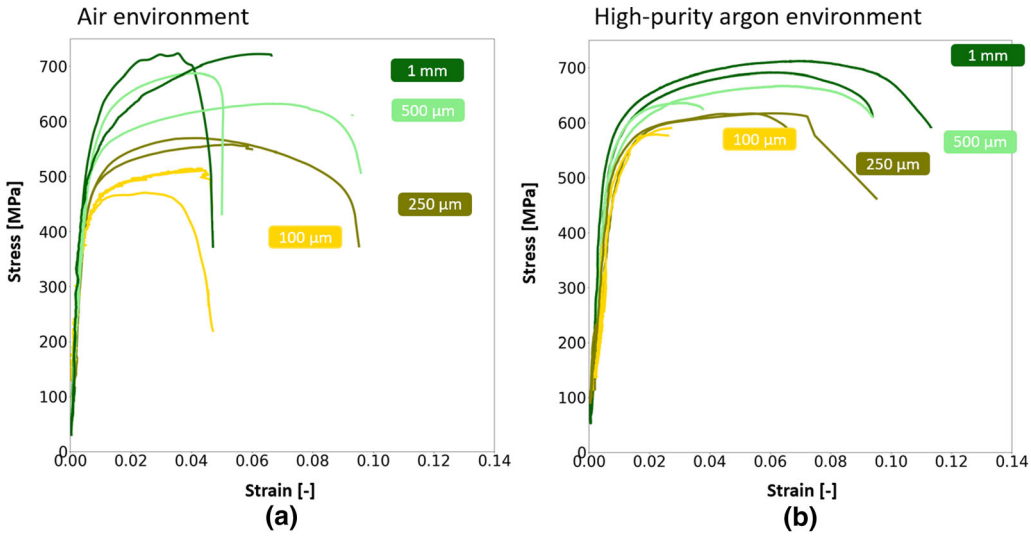

Fig. 5—True stress–strain curves at 550 °C under air (*a*) and under high-purity argon (*b*) for different specimen thicknesses.

Table IV. Young Modulus in GPa Values Determined at 550 °C for Each Thickness as a Function of Environment During Unloading

	1 mm	500 μm	250 μm	100 μm
Air	92	94	92	94
Argon	95	94	92	93

Young modulus determination technique induces error that can reach 4 GPa.

influence on the mechanical response of surface grains. This size effect is consistent with the transition from a polycrystalline to multicrystalline behavior described in References 2,6 with the transition located at a thickness above 1 mm. Free-surface grains are reported to have a different mechanical response than those in the core. Surface grains have a lower dislocation density due to a dislocation 'escape' through the free surface, which can delay the formation of dislocation cells, as shown by a TEM analysis in Reference 5 due to the absence of barrier preventing dislocation motion in the specimen for pure metals. The decrease in proportion and size of the dimpled area with decreasing specimen thickness supports these models. It should also be noted that a decrease in the number of colonies in specimen thickness induces a decrease in deformation incompatibilities between neighboring grains during tensile tests.[3] This constraining force caused by the interaction with adjacent colonies is no longer relevant for 100-μm-thick specimens. These two phenomena tend to diminish the formation of dislocation cells and therefore reduce yield stress due to surface colonies with a retarded work-hardening compared to core ones that will gradually impair macroscopic behavior.

In order to understand if size effects found in the present paper can be induced by a change from plane stress to plane strain due to change in specimen thickness-width-length ratio, finite element calculations (continuum mechanics) were performed to compare the

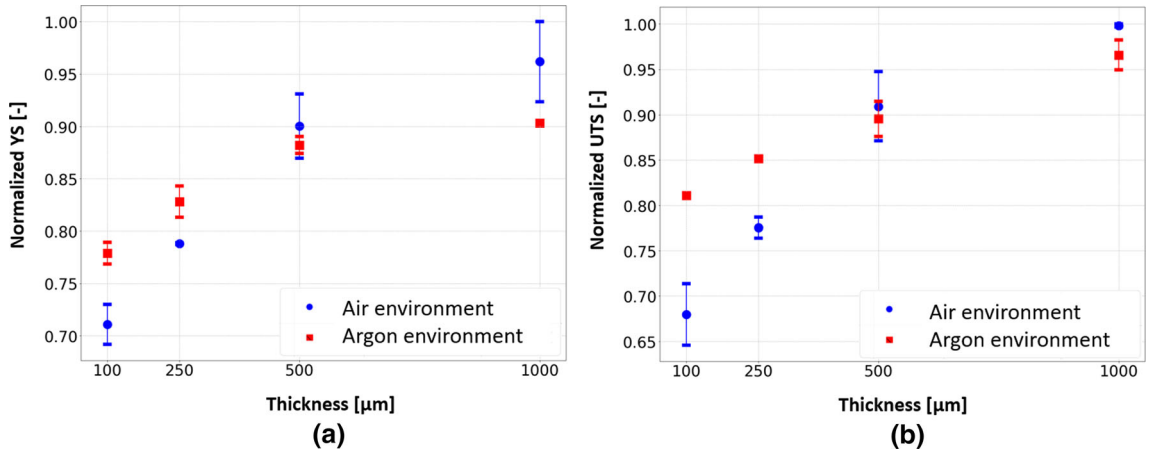

Fig. 6—Evolution of normalized Yield strength (YS) (*a*) and Ultimate Tensile Strength (UTS) (*b*) at 550 °C with the specimen thickness under air environment and under argon environment. The error bars correspond to the experimental dispersion of YS and UTS.

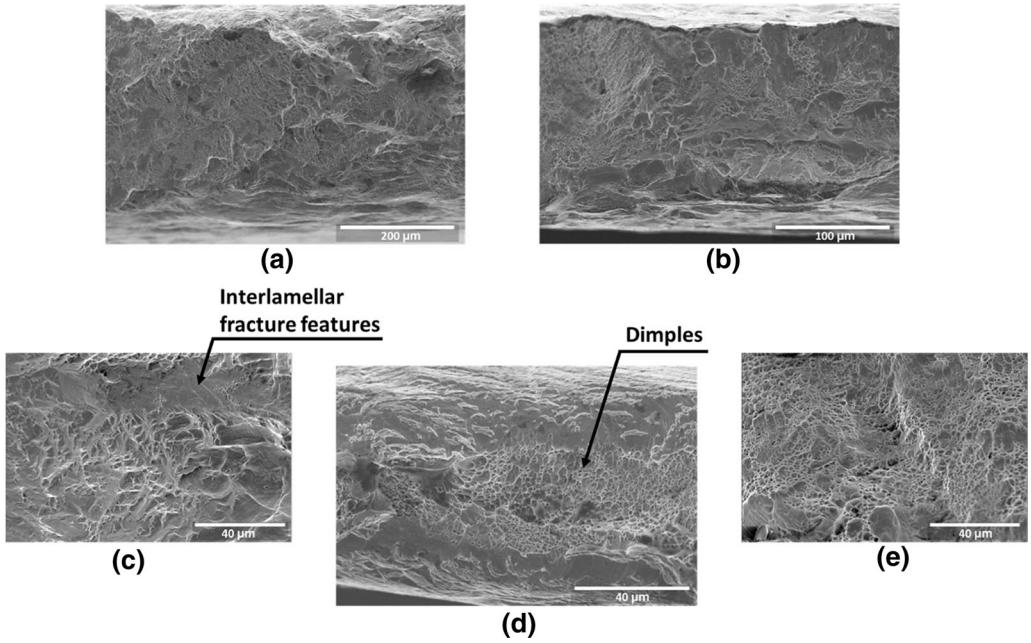

Fig. 7—SEM fractography of specimens with a thickness of 500 μm (*a*) and its dimpled area (*c*), 250 μm (*b*) and its dimpled area (*e*) and 100 μm (*d*) at $T = 450$ °C under air.

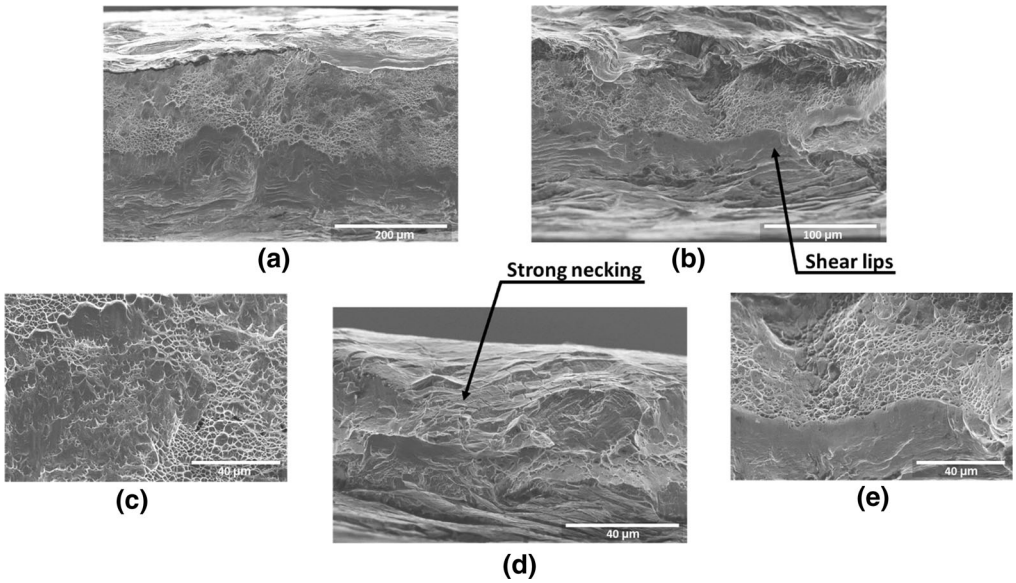

Fig. 8—SEM fractography of specimens with a thickness of 500 μm (*a*) and its dimpled area (*c*), 250 μm (*b*) and its dimpled area (*e*) and 100 μm (*d*) at $T = 550$ °C under air.

stress states at the core and the free surface of specimen with different thicknesses. These calculations were conducted for specimens with the two extreme geometries, *i.e.*, 0.1 and 1-mm-thick specimens. The variations of the stress states remained small for both the specimen geometries and negligible. A change in the stress state due to thickness decrease is not sufficient to explain the changes in the tensile curves, especially in the early plastic regime. A change in the local plasticity at the microstructure scale must therefore be considered instead and supports the progressive impact of surface colonies on the macroscopic mechanical behavior.

Due to the formation of an oxide layer at the surface, even a very thin one, the specimen surface cannot be considered as a real free surface when compared to previous literature studies in which specimens are tested at room temperature. This point will be developed in the following part.

B. *Influence of Oxidation*

Under air and static argon, specimens tested at high temperature are exposed to oxidation phenomena. First, the tests performed under air environment will be discussed. When temperature increases, oxidation affects a larger area of the initial section leading to a thicker external oxide layer and a thicker oxygen-enriched layer in the metal for an equal exposure duration. This affected area corresponds to less than 1 pct of the cross-section area at 550 °C and less than 0.1 pct at 450 °C for 100 μm specimens as described previously using data in References 43,49. The titanium oxide is formed at the metal/oxide interface due to the anionic oxidation mechanism. In the 0 MPa-applied stress situation, the metal to oxide transformation is accompanied by a 73 pct increase in volume (Pilling–Bedworth ratio equal to 1.73 for TiO_2/Ti[50]). The lateral growth of the oxide is partially constrained by the underlying metal. The oxide is thus in compression, whereas the alloy underneath, including the oxygen-enriched layer beneath the oxide, is subjected to tensile stresses. This configuration explains why the exposed surface is in a pre-constrained state as soon as the oxide starts to grow, *i.e.*, during heating and thermal dwelling until reaching a stabilized temperature. During these steps, specimens are maintained stressed by applying a moderate stress always below 150 MPa. The oxide layer, as well as the oxygen-enriched layer below the oxide scale continue to grow during the mechanical test under air environment. After the dwell time, according to Reference 43, the thickness of the oxygen-enriched layer is about 0.5 μm at 550 °C and about 0.07 μm at 450 °C. Furthermore, TEM observations have already been performed on specimens oxidized at the same temperature for longer periods (120 hours), confirming these orders of magnitude. On the other hand, EDS analyses carried out during these TEM observations did not reveal any oxygen enrichment at the interface of the α lamellae. These interfaces do not seem to be a privileged diffusion path as observed for TA6V.[51]

Observations of the specimens' surface reveal cracks in the oxide that are often perpendicular to the stress for all tested thicknesses.[52] These perpendicular cracks are comparable to those observed on tested tensile pre-oxidized specimens[53] and are induced by the presence of an oxide and/or an oxygen-enriched layer at the surface of the material. In Ward's results, when these tests were performed under vacuum, no surface cracks were evidenced.[52] These findings demonstrated the dynamic nature of embrittlement due to environment, and oxygen was assumed responsible for this effect. In Reference 54, crack depth was larger than the oxide layer thickness and crack tip was surrounded by a thin oxide layer. After crack opening, the freshly exposed underlying metal was subjected to oxidation and to further embrittlement thereby leading to another crack. By applying low strain rates, this embrittlement could be greater as the time exposure of the underlying metal is increased. The same mechanism could apply to this work. Assuming a progressive mechanism of crack propagation (which increases with temperature[55,56]) oxidation contributes to a reduction of the unaffected load-carrying cross-section. This loss would be faster for the thinnest specimens as surface oxidation does not depend on specimen thickness but only on temperature and environment. This could explain the loss of mechanical strength with decreasing thickness, as the crack size-to-specimen thickness ratio increases and also, the increase in mechanical strength properties drops with temperature, due to a greater oxidation. In addition, a decrease in the number of α lamellae colonies could also reduce the accommodation capability of the specimen core to propagation, and induce a greater propagation rate for the thinnest specimens. Considering short exposure durations at those temperatures, this scenario may not occur as interfaces did not act as short circuits for oxygen diffusion and cracks observed at the surface will be mainly due to plasticity as it will be explained later in this part. Oxygen dissolution could also modify the deformation of the α phase from a wavy to a planar slip mode due to the oxygen concentration increasing, as described in the study on pure titanium with various oxygen contents in Reference 57. This change, at local scale, could induce earlier strain localization and damage, which have a higher deleterious impact on the mechanical behavior of the thinnest specimens. The extrusion–intrusion mechanism described in Reference 26 could also damage the oxide layer as steps were observed in the surface of the thinnest specimens. The growth of oxide layer is very slow at the temperatures used in the present study. The external oxide scale is probably not homogeneous nor continuous due to a high interface density in this complex microstructure. Strain might be sufficiently intense (see *e.g.,* Reference 58) to locally crack the thin external oxide along the slip bands and recover the free-surface effect. This should lead to the commonly reported size effect due to retarded hardening in surface colonies compared to core colonies.

Under argon environment, a decrease in the mechanical strength of thinner samples is also highlighted as sample thickness decreases. The color of the specimen surface indicated that oxidation is strongly limited. Under argon, this surface coloration is slightly more visible for the thickest specimens and not visible on the 100-μm-thick sample. As oxidation depends on the partial pressure of oxygen in the furnace, the oxygen quantity is limited under pressurized argon, whereas under air, the quantity of oxygen is renewed. Assuming the quantity of oxygen is limited, the oxidation of the specimen and the grips will quickly consume the remaining oxygen thereby gradually reducing the oxygen content of the heating chamber.

Chong *et al.*[34] used pure titanium with various oxygen contents: [0.15 at.pct;0.88 at.pct]. These contents are much smaller compared to the oxygen content within the oxygen-enriched layer. Casadebaigt *et al.*[1]. showed on Ti–6Al–4V alloy that oxygen content varies between 0.2–0.3 at.pct and 12–25 at.pct in oxygen-enriched layer in temperature range [773–873 K]. Given the diffusion coefficient of oxygen at 450 and 550 °C, oxygen enrichment and strengthening observed by

Chong *et al.*[34] during the tensile test remain negligible even under air environment since oxygen-enriched layer corresponds to less than 1 pct of the gage section for the thinnest specimen. No core–shell effect due to sub-surface oxygen enrichment was observed at macroscopic level on the value of 0.2 pct offset yield strength and Young modulus. It is worth mentioning that the material exhibits similar values of Young modulus in air and argon. To explain the impact of environment on mechanical behavior, the role played by vacancies is considered. In the case of cationic growth of oxide scale, it is known and accepted that vacancies can be injected in the metal leading to void formation.[59] In the case of titanium, the mechanism of as oxidation is anionic but still as oxidation involves a Kirkendall effect[60] close to the metal/oxide interface, vacancy injection can occur during oxidation, as shown first by Dunnington.[61] This effect, both predicted and observed,[62–64] can increase the mobility of dislocations[65] and thus the plasticity near the surface, which is greater in air compared to argon environment. This may explain the differences between air and argon tests for thinner specimens, *i.e.*, lower yield strength values in air compared to argon despite a greater oxidation, which has a hardening effect.

C. *Influence of Dynamic Strain Aging*

Serrations highlighted at 450 °C are manifestations of dynamic strain aging (DSA). These serrations are explained by inhomogeneous deformations along the gage length,[66] and this jerky flow is called the Portevin Le Chatelier (PLC) effect. According to Reference 67, PLC serrations have the characteristics of C-type serrations. C-type serrations are associated with yield drops that occur below the general flow level and are considered to be due to dislocation unlocking. This effect can be explained as a consequence of the interaction between dislocations and solute atoms according to Reference 68 and was found to occur for pure titanium,[69,70] IMI 834,[66,71] and Ti6242S.[72] These types of serrations occur at high temperature and low strain rate. Jousset[72] defines the drag mode domain of DSA as the dominant one for the temperature domain and strain rate studied, where solute cloud is dragged by mobile dislocations. At high temperature, O, C, N, and H may cause this dynamic strain aging effect due to the high solubility of these solutes, as stated in Reference 73. In addition, according to Reference 66, substitutional atoms such as silicon can affect serrated behavior.

The influence of thickness decrease on the serrated behavior is investigated through the plastic strain at which DSA starts, the frequency, and amplitude of serrations (see Table III). First, the onset of serrations varies for a given thickness. As the number of colonies in the thickness decreases with specimen thickness, the t/d ratio decreases, which increases the influence of a single colony on the macroscopic behavior and on local heterogeneous strain distribution along the specimen gage. The sensitivity of tested specimen to α-Ti anisotropic elasto-plastic behavior is then enhanced as the sample thickness decreases compared to the polycrystalline situation. As aforementioned, Ti6242S microstructure can also be described by several microstructural lengths: lamella width, lamellae colony size, and former β-grain.

Mechanical anisotropy and heterogeneous deformation can also be described at different scales based on the crystallographic orientation of these microstructural features but also considering their morphological anisotropy. Despite DIC techniques were used to assess strain fields, full-field deformation maps did not allow us to evidence if localization observed is due to PLC bands or the heterogeneous strain distribution in former β-grains nor shear mechanisms in single colony. SEM surface analyses of tested specimens reveal intense slip bands at the surface. This plastic localization is strongly dependent on the crystallographic and morphological orientation of the α-colonies. At a larger scale, *i.e.*, at the former β-grain scale, 12 different variants of colonies are possible in one β-grain. EBSD analyses of tensile specimens before testing revealed 4 to 5 different variants in each former β-grain in the present study. Such microstructural features induce a heterogeneous distribution of strain, dislocations, and solute atoms in the material and therefore influence the onset of serrations for a given thickness. This anisotropy could explain the variability of the onset strain value and also the occurrence of this phenomenon for thick specimens ($t \geq 500$ μm). Specimen geometry also affects PLC effects, as described in Reference 74 in Al–Mg and Al–Mg-Mn alloys.[75] A decrease in thickness induces a change in specimen geometry as well as in strain distribution. This modification could also explain why PLC does not occur in 1-mm-thick specimens.

Plastic anisotropy can also induce strain incompatibility between neighboring colonies. A colony surrounded by other colonies can be more constrained than surface colonies, with more capability to freely deform *via* the free surface. The size of specimen will thus play a key role on the number of neighbors for an individual colony. In fact, larger is the sample, greater is strain incompatibility due to increase of colonies numbers. The density of mobile dislocations increases with strain level as described by Van den Beukel.[76] As explained in the first paragraph of the discussion section *"Influence of the size of α lamellae colonies compared to specimen thickness"*, it is assumed that the dislocation density and the size of dislocation cells decrease when sample thickness decreases, as it is observed on pure metals. In the usual case of polycrystalline situation, mobile dislocations interact with forest dislocations where solute atoms can gather. These interactions were investigated in Reference 77. The strain energy (proportional to strain and force) needed to overpass these obstacles increases with the size of forest of dislocations and gathered solute atoms quantity, which pin the mobile dislocations. This mechanism could explain the fact that the mean amplitude of serrations decreases with sample thickness due to a lower dislocation density, explained by lower constrained colonies. Unpinning of dislocations is therefore easier to overpass the first obstacle related to the onset of serrations. Moreover, DSA might concern all lamellae of the same α-colony at

a near moment during loading. Considering a low number of α colonies in a specimen, strain developed when the collective unpinning behavior occurs and is subsequently more visible at the macroscopic level for thin specimens. The glide of dislocations is easier, so they can move and interact with other solute atoms faster in thin specimens than in thick specimens. This might explain the higher DSA frequency in thinner sample. The same tendencies were observed in both environments.

Tensile tests performed under argon show a higher intensity of the DSA phenomenon, which is then evidenced on the 500-μm-thick specimen. Moreover, the amplitude of serrations is larger as compared to tests carried out in oxidizing conditions for the same geometry. The mobile dislocations are therefore more pinned under less oxidizing conditions. When stress increases, they glide again with a larger serration and then a greater stress decrease. As the quantity of interstitial atoms is not significantly modified, except at the extreme surface (< 500 nm) for tests carried out under air compared to those under argon, the main hypothesis relies on the role of vacancies in the dislocation motion: the lower oxidation under argon might induce a lower injection of vacancies, their diffusion can facilitate the mobility of dislocations. As these vacancies gradually annihilate in available sinks, their effect on macroscopic behavior is enhanced for tests carried out on thin samples.

Finally, one last point can be made in these results: the occurrence of DSA has a detrimental effect on ductility as showed in IMI 834,[71] which has a chemical composition similar to Ti6242S, as well as in pure titanium.[69,78,79] It is called the ''blue-brittle'' effect. A combination of oxidation phenomena and important DSA in thin specimens can explain the decrease in ductility with decreasing thickness.

Hence, environment seems to have an impact on the occurrence of DSA. The results obtained in this study allow us to formulate hypotheses, which can be further investigated in order to fully understand the mechanisms involved.

V. SUMMARY AND CONCLUSIONS

Tensile tests at 450 °C and 550 °C were performed on specimens with thickness varying from 1 mm to 100 μm with good reproducibility. The influence of sample thickness and oxidizing environment was investigated. The main conclusions of this work are as follows:

- A decrease in thickness leads to a decrease in mechanical strength at 450 and 550 °C. This loss of mechanical properties (yield strength, ultimate tensile strength) decreases as temperature increases. For thinner sample, changing from air to argon environment induces an increase in yield strength and ultimate tensile strength. The decrease of mechanical strength regardless of environment can be explained by the mechanical behavior of surface colonies, which gradually impairs specimen macroscopic mechanical behavior with thickness decreasing.
- Plastic strain is more heterogeneous in thinner samples due to microstructural aspects, potentially related to the former β-grain structure.
- Dynamic strain aging is highlighted at 450 °C with C-type serrations on thinner specimens. A decrease in mean load drop is observed with decreasing thickness for both environments. For thinner specimens, a higher serration frequency with lower serration amplitude is highlighted when changing from air to argon environment. This result could be explained by the difference in vacancy injection in the metal induced by environment modification, with a higher vacancy concentration enhancing dislocations mobility.
- It was also observed that a lower specimen thickness induces a significant modification of the fracture surface. When thickness decreases, a smaller area is dominated by dimples as necking is more and more pronounced.

These tests on thin specimens make it possible to highlight, on the one hand, the effects of specimen thickness on plastic behavior and, on the other hand, the dynamic effects of oxidation and DSA.

CONFLICT OF INTEREST

On behalf of all authors, the corresponding author states that there is no conflict of interest.

REFERENCES

1. A. Casadebaigt, J. Hugues, and D. Monceau: *Corros. Sci.*, 2020, vol. 175, p. 108875.
2. A.W. Thompson: *Scr. Metall.*, 1974, vol. 8, pp. 145–47.
3. S. Miyazaki, K. Shibata, and H. Fujita: *Acta Metall.*, 1979, vol. 27, pp. 855–62.
4. C. Keller and E. Hug: *Mater. Lett.*, 2008, vol. 62, pp. 1718–20.
5. C. Keller, E. Hug, R. Retoux, and X. Feaugas: *Mech. Mater.*, 2010, vol. 42, pp. 44–54.
6. C. Keller, E. Hug, and X. Feaugas: *Int. J. Plast.*, 2011, vol. 27, pp. 635–54.
7. M. Doner and J.A. Heckler: *Superalloys*, 1988, vol. 1988, pp. 653–62.
8. M.G.D. Geers, W.A.M. Brekelmans, and P.J.M. Janssen: *Int. J. Solids Struct.*, 2006, vol. 43, pp. 7304–21.
9. E. Hug, C. Keller, P.A. Dubos, and M.M. Celis: *J. Mater. Res. Technol.*, 2021, vol. 11, pp. 1362–77.
10. C. Romain, D. Texier, C. Desgranges, J. Cormier, S. Knittel, D. Monceau, and D. Delagnes: *Oxid. Met.*, 2021, vol. 96, pp. 169–82.
11. J.T. Fourie: *Philos. Mag.*, 1968, vol. 17, pp. 735–56.
12. H. Mughrabi: *Phys. Status Solidi*, 1971, vol. 44, pp. 391–402.
13. M.D. Uchic and D.M. Dimiduk: *Mater. Sci. Eng. A*, 2005, vol. 400–401, pp. 268–78.
14. J.R. Greer, W.C. Oliver, and W.D. Nix: *Acta Mater.*, 2005, vol. 53, pp. 1821–830.
15. C.A. Volkert and E.T. Lilleodden: *Philos. Mag.*, 2006, vol. 86, pp. 5567–579.
16. J.R. Greer and W.D. Nix: *Appl. Phys. A*, 2005, vol. 80, pp. 1625–629.
17. W.D. Nix: *Metall. Trans. A*, 1989, vol. 20, pp. 391–420.
18. R.-M. Keller, S.P. Baker, and E. Arzt: *J. Mater. Res.*, 1998, vol. 13, pp. 1307–317.

19. H. Huang and F. Spaepen: *Acta Mater.*, 2000, vol. 48, pp. 3261–269.
20. M. Hommel and O. Kraft: *Acta Mater.*, 2001, vol. 49, pp. 3935–947.
21. D.Y.W. Yu and F. Spaepen: *J. Appl. Phys.*, 2004, vol. 95, pp. 2991–997.
22. A.A. Benzerga and N.F. Shaver: *Scr. Mater.*, 2006, vol. 54, pp. 1937–941.
23. R. Venkatraman and J.C. Bravman: *J. Mater. Res.*, 1992, vol. 7, pp. 2040–48.
24. A. Srivastava, S. Gopagoni, A. Needleman, V. Seetharaman, A. Staroselsky, and R. Banerjee: *Acta Mater.*, 2012, vol. 60, pp. 5697–711.
25. M. Brunner, M. Bensch, R. Völkl, E. Affeldt, and U. Glatzel: *Mater. Sci. Eng. A*, 2012, vol. 550, pp. 254–62.
26. B. Cassenti and A. Staroselsky: *Mater. Sci. Eng. A*, 2009, vol. 508, pp. 183–89.
27. W.L. Finlay and J.A. Snyder: *JOM*, 1950, vol. 2, pp. 277–86.
28. J. Baillieux, D. Poquillon, and B. Malard: *J. Appl. Crystallogr.*, 2016, vol. 49, pp. 175–81.
29. G. Baur and P. Lehr: *J. Less-Common Met.*, 1980, vol. 69, pp. 203–18.
30. M. Yan, W. Xu, M.S. Dargusch, H.P. Tang, M. Brandt, and M. Qian: *Powder Metall.*, 2014, vol. 57, pp. 251–57.
31. F.B. Vicente, D.R.N. Correa, T.A.G. Donato, V.E. Arana-Chavez, M.A.R. Buzalaf, and C.R. Grandini: *Materials (Basel)*, 2014, vol. 7, pp. 542–53.
32. D. Texier, Q. Sirvin, V. Velay, M. Salem, D. Monceau, B. Mazères, E. Andrieu, R. Roumiguier, and B.B. Dod: *Titanium 2019*, 2020, pp. 0–4.
33. B. Barkia, J.P. Couzinié, S. Lartigue-Korinek, I. Guillot, and V. Doquet: *Mater. Sci. Eng. A*, 2017, 703, vol. 703.
34. Y. Chong, M. Poschmann, R. Zhang, S. Zhao, M.S. Hooshmand, E. Rothchild, D.L. Olmsted, J.W. Morris, D.C. Chrzan, M. Asta, and A.M. Minor: *Sci. Adv.*, 2020, vol. 6, pp. 1–11.
35. P. Stratton: *Int. Heat Treat. Surf. Eng.*, 2013, vol. 7, pp. 70–73.
36. M. Zupan and K.J. Hemker: *Mater. Sci. Eng. A*, 2001, vol. 319–321, pp. 810–14.
37. M. Zupan, D.M. Dimiduk, and K.J. Hemker: *MRS Online Proc. Libr.*, 1999, vol. 552, pp. 1–6.
38. R.R. Boyer: *Mater. Sci. Eng. A*, 1996, vol. 213, pp. 103–14.
39. R. Gaddam, B. Sefer, R. Pederson, and M.L. Antti: *IOP Conf. Ser. Mater. Sci. Eng.*, 2002, vol. 48, p. 1.
40. D. Texier, D. Monceau, J.C. Salabura, R. Mainguy, and E. Andrieu: *Mater. High Temp.*, 2016, vol. 33, pp. 325–37.
41. D. Lunt, X. Xu, T. Busolo, J. Quinta da Fonseca, and M. Preuss: *Scr. Mater.*, 2018, vol. 145, pp. 45–49.
42. M.A. Sutton, J.J. Orteu, and H.W. Schreier: *Image Correlation for Shape, Motion and Deformation Measurements: Basic Concepts Theory and Applications*, Springer, Boston, 2009.
43. N. Vaché, Y. Cadoret, B. Dod, and D. Monceau: *Corros. Sci.*, 2021, vol. 178, p. 109041.
44. C.A. Schneider, W.S. Rasband, and K.W. Eliceiri: *Nat. Methods*, 2012, vol. 9, pp. 671–75.
45. M. Surand. Institut National Polytechnique de Toulouse. PhD Thesis, Université de Toulouse, 2013.
46. J. Baillieux. Institut National Polytechnique de Toulouse. PhD Thesis, Université de Toulouse, 2015.
47. E. Hug and C. Keller: *Metall. Mater. Trans. A*, 2010, 41, 2498–506.
48. C. Keller, E. Hug, and D. Chateigner: *Mater. Sci. Eng. A*, 2009, vol. 500, pp. 207–15.
49. R.N. Shenoy, J. Unnam, and R.K. Clark: *Oxid. Met.*, 1986, vol. 26, pp. 105–24.
50. H.E. Evans: *Int. Mater. Rev.*, 1995, vol. 40, pp. 1–40.
51. A. Casadebaigt, D. Monceau, and J. Hugues: *MATEC Web Conf.*, 2020, vol. 321, p. 03006.
52. C.H. Ward, A.W. Thompson, and J.C. Williams: *Scr. Metall. Mater.*, 1993, vol. 28, pp. 1017–21.
53. T.A. Parthasarathy, W.J. Porter, S. Boone, R. John, and P. Martin: *Scr. Mater.*, 2011, vol. 65, p. 65.
54. R.S. Mishra, D. Bannerjee, and A.K. Mukherjee: *Mater. Sci. Eng. A*, 1995, vol. 192–193, pp. 763–68.
55. C.H. Ward, A.W. Thompson, and J.C. Williams: *Metall. Mater. Trans. A*, 1995, vol. 26, pp. 703–20.
56. R. Foerch, A. Madsen, and H. Ghonem: *Metall. Trans. A*, 1993, vol. 24, pp. 1321–332.
57. J.C. Williams, A.W. Sommer, and P.P. Tung: *Metall. Trans.*, 1972, vol. 3, pp. 2979–984.
58. M.P. Echlin, J.C. Stinville, V.M. Miller, W.C. Lenthe, and T.M. Pollock: *Acta Mater.*, 2016, vol. 114, pp. 164–75.
59. C. Desgranges, F. Lequien, E. Aublant, M. Nastar, and D. Monceau: *Oxid. Met.*, 2013, vol. 79, pp. 93–105.
60. A.D. Smigelskas and E.O. Kirkendall: *Trans. AIME*, 1947, vol. 171, pp. 130–42.
61. B.W. Dunnington, F.H. Beck, and M.G. Fontana: *Corrosion*, 1952, vol. 8, pp. 2–12.
62. R. Francis and D.G. Lees: *Mater. Sci. Eng. A*, 1989, vol. 120–121, pp. 97–99.
63. S. Perusin, B. Viguier, D. Monceau, L. Ressier, and E. Andrieu: *Acta Mater.*, 2004, vol. 52, pp. 5375–80.
64. C.M. Wang, A. Genc, H. Cheng, L. Pullan, D.R. Baer, and S.M. Bruemmer: *Sci. Rep.*, 2015, vol. 4, pp. 1–6.
65. S. Dryepondt, D. Monceau, F. Crabos, and E. Andrieu: *Acta Mater.*, 2005, vol. 53, pp. 4199–4209.
66. K. Prasad and V.K. Varma: *Mater. Sci. Eng. A*, 2008, vol. 486, pp. 158–66.
67. P. Rodriguez: *Bull. Mater. Sci.*, 1984, vol. 6, pp. 653–63.
68. A.H. Cottrell: *Philos. Mag.*, 1953, vol. 44, pp. 829–32.
69. A.M. Garde, A.T. Santhanam, and R.E. Reed-Hill: *Acta Metall.*, 1972, vol. 20, pp. 215–20.
70. M. Doner and H. Conrad: *Metall. Trans.*, 1973, vol. 4, pp. 2809–17.
71. K. Prasad: *Mater. Sci. Technol.*, 2010, vol. 26, pp. 1068–72.
72. H. Jousset. École Nationale Supérieure des Mines de Paris. PhD Thesis, 2008.
73. H. Conrad: *Prog. Mater. Sci.*, 1981, vol. 26, pp. 123–403.
74. J.M. Robinson and M.P. Shaw: *Mater. Sci. Eng. A*, 1992, vol. 159, pp. 159–65.
75. J. Zdunek, W.L. Spychalski, J. Mizera, and K.J. Kurzydłowski: *Mater. Charact.*, 2007, vol. 58, pp. 46–50.
76. A. van den Beukel: *Phys. Status Solidi*, 1975, vol. 30, pp. 197–206.
77. A. Van Den Beukel and U.F. Kocks: *Acta Metall.*, 1982, vol. 30, pp. 1027–34.
78. A.T. Santhanam and R.E. Reed-Hill: *Metall. Trans.*, 1971, vol. 2, pp. 2619–22.
79. O.N. Senkov and J.J. Jonas: *Metall. Mater. Trans. A*, 1996, vol. 27, pp. 1877–87.